PHYSICAL REVIEW A **88**, 023409 (2013)

Spatial interferences of photodetachment near a repulsive center

B. C. Yang,[1] J. B. Delos,[2] and M. L. Du[1,*]
[1]*State Key Laboratory of Theoretical Physics, Institute of Theoretical Physics, Chinese Academy of Science, Beijing 100190, China*
[2]*Physics Department, College of William and Mary, Williamsburg, Virginia 23185, USA*

(Received 22 May 2013; published 6 August 2013)

We study the detached-electron flux distributions from the photodetachment of a negative ion near a repulsive center. Using a semiclassical approach, we calculate the electron flux on spherical detectors with various radii. The classically allowed angular range of the interference patterns on the spherical screen increases as the detached-electron energy is increased. In the classically allowed range, we find that there are always two trajectories going from the negative ion to the observation point on the screen, inducing quantum interference patterns. We have also extended the formulas into the tunneling region. The interference patterns also reflect the quantum angular distribution of electrons leaving the ion. A scaling property for the detached-electron flux is investigated. The accuracy of our semiclassical formulas is established by comparison with a quantum treatment using the exact Coulomb Green's function.

DOI: 10.1103/PhysRevA.88.023409 PACS number(s): 32.80.Gc, 31.15.xg

I. INTRODUCTION

Angle-resolved photoelectron spectra from doubly charged anions having the structure of a linear chain, $^{-}O_2C-(CH_2)_m-CO_2{}^{-}$ (with $3 \leqslant m \leqslant 11$), have recently been observed experimentally [1]. These experiments are an interesting extension of photoelectron microscopy, for which the theory was first developed by Fabrikant, Demkov and Du [2–4], and which was first implemented by Blondel and his co-workers [5]. Inspired by the above studies, we explore in this paper photodetachment of electrons from certain types of doubly charged anions, $h\nu + \mathrm{M}^{-2} \rightarrow \mathrm{M}^{-1} + e^{-}$. Specifically, we consider differential cross section for photodetachment of electrons from one negative ion that is close to another negative ion. In our theoretical model (Fig. 1), the loosely bound electron is detached by absorption of a single photon, and it escapes out the repulsive force field provided by the other negative ion. Deviations from the predictions of this simple model would be related to interactions of the escaping electron with the neutral framework of the molecule or polarization of the residual molecular ion.

We have previously examined photodetachment from singly charged atomic anions in an electric field [6] and in parallel or perpendicular electric and magnetic fields [7]. Related experiments have been reported [8], and other theoretical methods can also be found in [9]. In that work, interference oscillations were found in the differential and total cross sections. Those in the differential cross section result from waves traveling along various paths from source to detector. Oscillations in the total cross section arise from interference of outgoing and returning waves, going from source to source. The general framework describing these interference structures is called closed-orbit theory, which was initially developed to deal with the quasi-Landau resonances in the photoionization of atom in a magnetic field by Delos and Du [10].

The present study is a natural extension of that work. Instead of an externally imposed uniform electric field, the negatively charged center provides a repulsive central field. Electrons are emitted from a "source" anion, and follow paths governed by the repulsive Coulomb field around the other negative ion. The problem is like Rutherford scattering, except that the paths begin from a point source close to the charged target. The detached-electron wave can be constructed using a semiclassical approximation by propagating classical paths from source to detector. We will see that either zero or two paths go from the source anion to a given location on a detector, and a simple interference pattern is found in the differential cross section.

This is a system for which an exact wave function can be obtained in closed form, because the Coulomb Green's function can be written in terms of Whittaker functions of the first and second kinds [11,12]. It turns out, however, that this seemingly simple expression [Eq. (E1) in our Appendix E] is not very informative—we have not extracted any meaningful physics from it. In contrast, the semiclassical approximation gives a clear intuitive picture of flow along a family of hyperbolic orbits; it delineates classically allowed from classically forbidden regions; it involves nothing more complex than the trigonometric integrals that are characteristic of repulsive Coulomb systems; in addition the semiclassical computations require less computer time than the exact computations.

In most of our calculation, a "primitive" semiclassical approximation is sufficient. However, as is well known, the primitive semiclassical approximation diverges near any boundary between classically allowed and forbidden regions. We repair this divergence using Airy-function formulas. The accuracy of the semiclassical formulas is shown to be excellent through comparison with the exact Coulomb Green's function for an s-wave source.

The remainder of this article is organized as follows. In Sec. II, the theoretical model for photodetachment of electrons from a negative ion near a fixed negatively charged center is described, and the classical motion of the detached electron in the repulsive central field is described quantitatively. In Sec. III, we use these trajectories to compute the semiclassical approximation to the electron waves. In Sec. IV, the electron flux is calculated for the classically accessible region away from the boundary of classical motion. Then we correct the wave function near the caustic surface and extend it into the classically forbidden region. In Sec. V, calculations are

---

[*] duml@itp.ac.cn

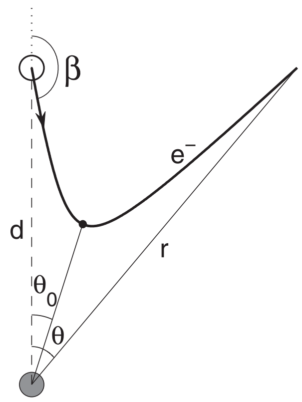

FIG. 1. Schematic representation of the theoretical model for the scattering of electrons outgoing from a point source by a repulsive force center. The open and solid circles denote the electron source and the negatively charged center, respectively. The electron source is supplied by the photodetachment of the negative ion. After the electron is detached by a photon, it escapes following a hyperbolic trajectory as shown by the heavy solid curve on which a dark point indicates the closest point to the force center.

displayed for representative cases, and several important and interesting aspects are discussed. In Sec. VI, a brief conclusion is given. Atomic units are used throughout this work unless specified otherwise.

II. THEORETICAL MODEL AND CLASSICAL TRAJECTORY STRUCTURE

Here we set out the basic aspects of the theoretical model (Fig. 1): Photodetachment of electrons from a singly charged atomic anion near a second anion that acts as a fixed repulsive force center. We set the z axis along the line connecting the ions and the force center. When a laser light is applied, the loosely bound electron may be detached, leaving a neutral atom behind. The electron goes into a spherically outgoing wave,

$$\psi_{\text{out}}(R,\beta,\phi) = C(k)Y_{lm}(\beta,\phi)\frac{e^{ikR}}{R}, \tag{1}$$

where (R,β,ϕ) are spherical coordinates for the electron relative to the residual neutral atom, that is, the source point; $C(k)$ is a factor dependent on the electron energy E, and $k = \sqrt{2E}$. The angle-dependent factor $Y_{lm}(\beta,\phi)$ is a spherical harmonic function representing the angular distribution of outgoing waves. The specific expression for this source wave can be calculated for the specific ion and various laser polarizations [4,6]. Thereafter, the theoretical model is simply *scattering of an electron wave emerging at fixed energy from a point source by a fixed repulsive force center.*

Polar coordinates $(r,\, \theta)$ centered at the force center are a better choice for describing the electron motion. We set the polar axis along the positive z axis (from the force center toward the source of electrons), and θ is the corresponding polar angle. We also select the source point to be the zero-potential-energy point. Then the Hamiltonian governing the motion of detached electron can be written as

$$H = \frac{p_r^2}{2} + \frac{p_\theta^2}{2r^2} + \frac{\alpha}{r} - \frac{\alpha}{d}, \tag{2}$$

where d is the distance between the wave source and the repulsive center, and α denotes the negative-charge number at the force center. The last term is a constant and it makes the potential energy zero at the source.

We introduce the scaled energy $\widetilde{E} = Ed/\alpha$, which is the only parameter determining the shape of the electron trajectory when the position of the detector is fixed. It is convenient to define also two complementary parameters $\xi > 0$ and $\eta > 0$ as

$$\xi^2 = \frac{2p_0^2}{p_\infty^2 - p_0^2} = 2\widetilde{E}; \tag{3}$$

$$\eta^2 = \frac{2p_\infty^2}{p_\infty^2 - p_0^2} = 2(\widetilde{E} + 1), \tag{4}$$

using the magnitude of the initial momentum $p_0 = \sqrt{2E} = k$ and the final momentum at infinity $p_\infty = \sqrt{2(E + \alpha/d)}$. Following the standard method usually applied for the Kepler problem in classical mechanics [13], the orbit equation of the Hamiltonian in Eq. (2) can be written as

$$r = \left(\frac{\xi^2 \sin^2(\beta)}{\varepsilon \cos(\theta - \theta_0) - 1}\right)d, \tag{5}$$

where ε is the eccentricity of the hyperbolic orbit (Fig. 1),

$$\varepsilon = \sqrt{1 + \xi^2\eta^2 \sin^2(\beta)}, \tag{6}$$

and θ_0 is the polar angle of the nearest point to the force center, which can be written as

$$\theta_0 = \begin{cases} \frac{\pi}{2} - \arcsin\left(\frac{1+\xi^2\sin^2(\beta)}{\varepsilon}\right) & \text{if} \quad \beta > \frac{\pi}{2}, \\ -\frac{\pi}{2} + \arcsin\left(\frac{1+\xi^2\sin^2(\beta)}{\varepsilon}\right) & \text{if} \quad \beta \leqslant \frac{\pi}{2}. \end{cases} \tag{7}$$

The orbit equation in Eq. (5) contains all the information needed in the following discussions.

As a result of the cylindrical symmetry of the present system, we only need to describe the trajectories in the right half plane in Fig. 1. On the other hand, due to the central field property, the natural choice to collect the scattered electron is a spherical detector centered at the force center. Hence, spherical coordinates (r,θ,φ) relative to the force center will be adopted in the following analyses (Fig. 1).

Giving a point (r,θ), the condition for the existence of real roots β of orbit equation can be obtained from Eq. (5),

$$\delta = (\widetilde{E} + 1)^2 \cos(\theta) + \widetilde{E}^2 - 1 - 2\widetilde{E}\frac{d}{r} \geqslant 0, \tag{8}$$

which gives the classically accessible region of the plane (Appendix A). The caustic (the boundary between allowed and forbidden regions) occurs where the discriminant equals zero:

$$r = \frac{2\widetilde{E}d}{(\widetilde{E} + 1)^2 \cos(\theta) + \widetilde{E}^2 - 1}, \quad 0 \leqslant \theta < \arccos\left(\frac{1 - \widetilde{E}}{1 + \widetilde{E}}\right), \tag{9}$$

which is also a hyperbola.

Structures for the classical trajectory pattern can be found from the caustic equation (Fig. 2). If $0 < \widetilde{E} < 1$ [Fig. 2(a)], the hyperbolic caustic curves upward, and electrons emitted in any direction are turned back to the positive z direction. When $\widetilde{E} = 1$ [Fig. 2(b)], the caustic surface becomes a plane located

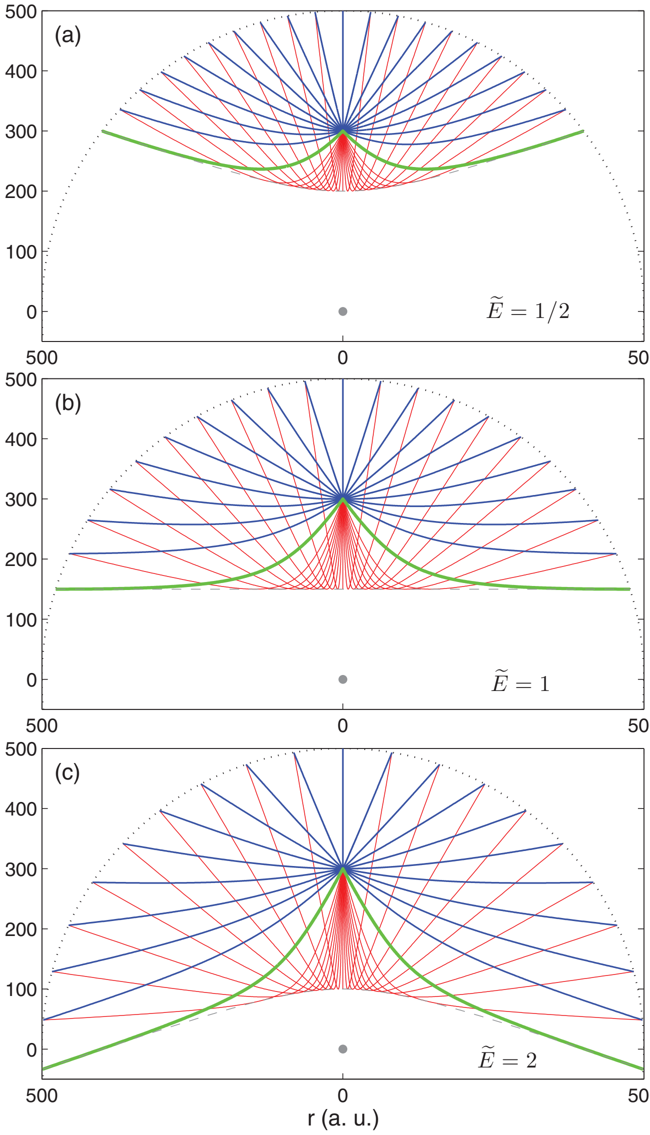

FIG. 2. (Color online) Three typical trajectory patterns determined by the scaled energy $\widetilde{E}$; here $d = 300a_0$, $\alpha = 1$, $r = 500a_0$, and a_0 is the Bohr radius. For each point in the classically allowed region on the spherical detector with radius r, there are always two trajectories with different initial angles β_1 and β_2. The initial angle β is indicated in Fig. 1. At the classically allowed region boundary θ_m on the spherical detector, the two trajectories become identical as represented by the green and thick curve. The caustic surface is given by the dashed line.

at $z = d/2$ and the plane bisects the line between the source point and the force center. If $\widetilde{E} > 1$ [Fig. 2(c)], the hyperbolic caustic curves downward.

With the help of an expression for the spherical angle from Eq. (5),

$$\theta = \theta_0 + \arccos\left(\frac{1 + \frac{d}{r}\xi^2\sin^2(\beta)}{\varepsilon}\right), \quad r > d, \tag{10}$$

and its asymptotic value when $r \to \infty$,

$$\theta_\infty = \theta_0 + \arccos\frac{1}{\varepsilon},$$

we can further depict the details of the three different trajectory structures. Specifically, as illustrated in Fig. 2(a), all the detached-electron trajectories with scaled energy $\widetilde{E} < 1$ are turned back to the upward direction. In the second case when $\widetilde{E} = 1$ [Fig. 2(b)], electron trajectories are turned back to the positive z direction except for the one trajectory with initial angle $\beta = 3\pi/4$ which propagates toward the midperpendicular plane, approaching the caustic surface asymptotically as $r \to \infty$. In the third case when $\widetilde{E} > 1$ [Fig. 2(c)], only the trajectories with the initial angle falling in the interval $[0,\beta_1^b)$ or $(\beta_2^b,\pi]$ are turned back to the upward direction, while the trajectories with the initial angle between $\beta_1^b = \frac{\pi}{2} + \frac{1}{2}\arcsin(\frac{1}{\widetilde{E}})$ and $\beta_2^b = \pi - \frac{1}{2}\arcsin(\frac{1}{\widetilde{E}})$ propagate downward and end in the lower half plane. The two trajectories with the initial angles equal to β_1^b and β_2^b go out downward initially, and finally go out horizontally with $z = L/\sqrt{2(E + \alpha/d)}$ at $r \to \infty$, where $L = kd\sin\beta$ is the angular momentum in the spherical coordinates.

The caustic equation Eq. (8) also gives us the maximum θ value on the spherical detector,

$$\theta_m = \arccos\left(\frac{2\widetilde{E}\frac{d}{r} - (\widetilde{E}^2 - 1)}{(\widetilde{E} + 1)^2}\right), \tag{11}$$

which then tells us the range of the interference pattern on the spherical detector. Another special and important angle corresponds to the trajectory with initial angle $\beta = \pi/2$, which can be calculated specifically after Eq. (10),

$$\theta_c = \arccos\left(\frac{1 + 2\widetilde{E}\frac{d}{r}}{1 + 2\widetilde{E}}\right). \tag{12}$$

Finally, when we solve the orbit equation in Eq. (5), we find that for each point on the detector in the classically accessible region, there are always two trajectories, and they came from initial angles β_1 and β_2, given by the following formulas (Appendix A).

$$\beta_1 = \pi - \arcsin(\sqrt{x_1}), \tag{13}$$

where

$$x_1 = (1 - \cos\theta) \times \frac{\frac{\widetilde{E}+1}{2}\left(\sqrt{1+\cos\theta} - \sqrt{\cos\theta - \cos\theta_m}\right)^2 - \frac{1}{\widetilde{E}+1}\frac{d}{r}}{(2\widetilde{E}+1)\left(1 - \frac{d}{r}\right)(1 - \cos\theta_c) + 4\widetilde{E}\frac{d}{r}(1 - \cos\theta)}. \tag{14}$$

$$\beta_2 = \begin{cases} \arcsin(\sqrt{x_2}) & \text{if} \quad 0 \leqslant \theta \leqslant \theta_c, \\ \pi - \arcsin(\sqrt{x_2}) & \text{if} \quad \theta_c < \theta \leqslant \theta_m, \end{cases} \tag{15}$$

where

$$x_2 = (1 - \cos\theta) \times \frac{\frac{\widetilde{E}+1}{2}\left(\sqrt{1+\cos\theta} + \sqrt{\cos\theta - \cos\theta_m}\right)^2 - \frac{1}{\widetilde{E}+1}\frac{d}{r}}{(2\widetilde{E}+1)\left(1 - \frac{d}{r}\right)(1 - \cos\theta_c) + 4\widetilde{E}\frac{d}{r}(1 - \cos\theta)}. \tag{16}$$

The above analysis is illustrated in Fig. 2 and in more detail in Fig. 3. With the detection position θ away from the z axis, the initial angle β_2 for the up (blue online) trajectory increases from 0°, meanwhile, the initial angle β_1 for the down (red online) trajectory decreases from 180°. When the detection

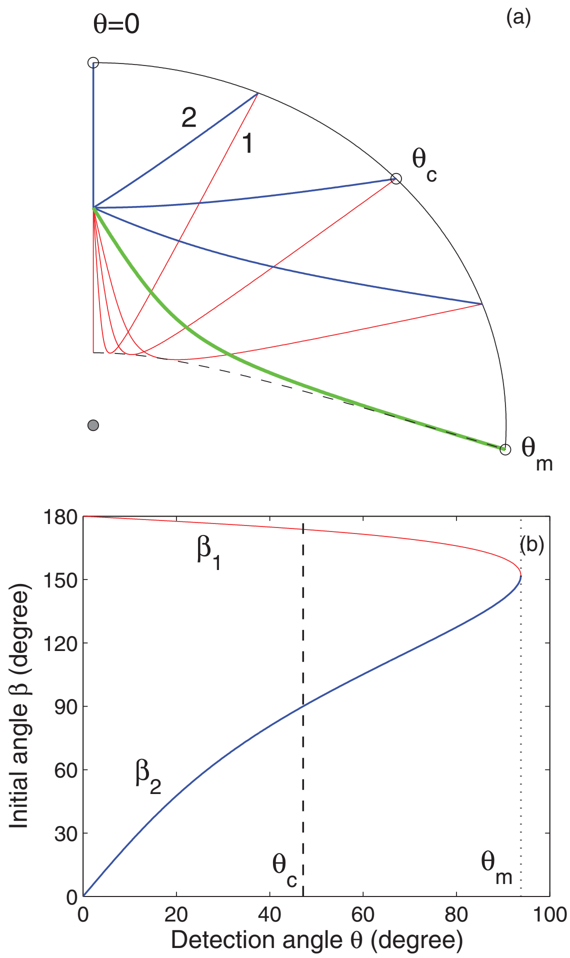

FIG. 3. (Color online) (a) Details of the electron trajectories in Fig. 2(c); (b) initial angles for the two trajectories vs the detection angle on the spherical detector.

position reaches the caustic θ_m, the two trajectories coincide, $\beta_1 = \beta_2$, which is indicated by the green trajectory in Figs. 2 and 3.

Here we also mention that both of the initial angles for the trajectories reaching the detector between θ_c and θ_m are larger than $\pi/2$; this will have an effect on the electron flux that will be discussed in the following section.

III. SEMICLASSICAL WAVE PROPAGATION

A. Quantum wave construction from classical trajectories

The standard method for constructing a quantum wave function from classical trajectories is given in Ref. [14]. Assuming the wave function on an initial spherical surface is given by $\psi_{\text{out}}(R,\beta,\varphi)$, then the semiclassical wave for the present cylindrical case can be constructed as

$$\psi(r,\theta,\varphi) = \sum_\nu \psi_{\text{out}}(R,\beta_\nu,\varphi) A_\nu \exp\left[i\left(S_\nu - \mu_\nu \frac{\pi}{2}\right)\right], \quad (17)$$

where the summation is over all trajectories arriving at the final point (r,θ,φ), and ν is the label for those trajectories. S_ν is the classical action,

$$S_\nu = \int \mathbf{p}\cdot d\mathbf{q}, \quad (18)$$

along the ν^{th} trajectory from the initial surface to any given final point on that trajectory, and μ_ν is the corresponding Maslov index. The semiclassical amplitude A_ν is defined as

$$A_\nu = \left|\frac{J(t=0)}{J(t=T)}\right|^{1/2}, \quad (19)$$

and

$$J(t) = \det\left(\frac{\partial(x,y,z)}{\partial(t,\beta,\phi)}\right), \quad (20)$$

evaluated at the initial and final points, (x,y,z), and at $\beta = \beta_\nu$ (the initial angles for the ν^{th} trajectory). We call this quantity the classical Jacobian.

B. Amplitude reduction

Given the cylindrical symmetry of the present system, we first reduce the above classical Jacobian to two dimensions [10],

$$J(t) = r^2 \sin\theta \det\left(\frac{\partial(r,\theta)}{\partial(t,\beta_\nu)}\right). \quad (21)$$

The difficulty to obtain the Jacobian is the calculation of the determinant on the right side of Eq. (21), which is always encountered in the present studies. We find the above two-dimensional Jacobian Eq. (21) can be actually reduced to (Appendix B)

$$J(t) = p_r r^2 \sin\theta \left(\frac{\partial\theta}{\partial\beta_\nu}\right)_r. \quad (22)$$

The partial derivative $(\frac{\partial\theta}{\partial\beta_\nu})_r$ can be calculated straightforwardly from Eq. (10) as (Appendix C)

$$\left(\frac{\partial\theta}{\partial\beta_\nu}\right)_r = 1 + \frac{1-\eta^2}{\varepsilon^2} + \frac{\eta^2 - \frac{d}{r}(1+\varepsilon^2)}{\varepsilon^2} \times \frac{k}{p_r}\cos\beta_\nu, \quad (23)$$

where

$$p_r = \sqrt{2\left(E - \frac{L^2}{2r^2} - \frac{\alpha}{r} + \frac{\alpha}{d}\right)}$$

is the radial momentum with initial angle β_ν.

For the Jacobian at $t = 0$, one can readily show

$$J(t=0) = kR^2 \sin\beta_\nu. \quad (24)$$

Therefore we obtain

$$A_\nu = \left|\frac{kR^2\sin\beta_\nu}{p_r r^2 \sin\theta \left(\frac{\partial\theta}{\partial\beta_\nu}\right)_r}\right|^{1/2}, \quad (25)$$

and, if $\theta = 0$, we have

$$A_\nu = \frac{R}{r} \times \sqrt{\frac{k}{p_r}} \times \frac{1}{\left|\left(\frac{\partial\theta}{\partial\beta_\nu}\right)_r\right|}. \quad (26)$$

When the detection distance r is chosen and fixed, the detection angle θ is a function of β. To simplify the notations, the partial derivative $(\frac{\partial\theta}{\partial\beta_\nu})_r$ can be denoted as $\frac{d\theta}{d_\beta}$. Thereafter, we can write the amplitude in Eq. (25) as

$$A = \left|\frac{kR^2 \sin\beta d\beta}{p_r r^2 \sin\theta d\theta}\right|^{1/2}, \tag{27}$$

at a spherical detector of radius r, where the subscript ν is omitted.

The result in Eq. (27) can be understood by considering the following electron-flow process. Assuming, near a differential area $(R^2 \sin\beta d\beta d\phi)$ on the initial sphere, the electron number density is $\rho_e(R,\beta,\phi)$. Then, the total electron number dN streaming through the initial differential area per unit time can be obtained as

$$dN = \rho_e(R,\beta,\phi)kR^2 \sin\beta d\beta d\phi. \tag{28}$$

These electrons will flow through the corresponding differential area $(r^2 \sin\theta|d\theta|d\varphi)$ on the final spherical detector, and the same argument gives the total electron number as

$$dN = \rho_e(r,\theta,\varphi)p_r r^2 \sin\theta|d\theta|d\varphi. \tag{29}$$

Given the cylindrical symmetry of the present system, the ratio of Eq. (29) to Eq. (28) gives us

$$\left|\frac{kR^2 \sin\beta d\beta}{p_r r^2 \sin\theta d\theta}\right| = \frac{\rho_e(r,\theta,\varphi)}{\rho_e(R,\beta,\phi)}. \tag{30}$$

Based on the above discussion, we have

$$A = \sqrt{\frac{\rho_e(r,\theta,\varphi)}{\rho_e(R,\beta,\phi)}}. \tag{31}$$

Finally, we reach the specific physical meaning of the constructed amplitude: *the constructed-amplitude square along the classical trajectory is actually the ratio of the particle density on the final position to that on the wave-source location*. This physical interpretation, which is consistent with the Born's probability interpretation of the quantum matter wave, ensures that the constructed semiclassical wave is reasonable.

C. Phase accumulation

The semiclassical phase accumulation is dependent on the Maslov index and the action variation. The Maslov index can be obtained from the classical trajectory structure, and the classical action can also be calculated analytically after some manipulations.

According to the trajectory analyses in Sec. II (Figs. 2 and 3), the down (red) trajectory "1" has one touch with the caustic surface, and the corresponding Maslov index $\mu_1 = 1$, while, the up (blue) trajectory "2" has no touch with the caustic surface and $\mu_2 = 0$.

For an electron ejected with an initial angle β, arriving at the final spherical detector of radius r, the action variation can be expressed as a function of β and r, that is, $S(r,\beta)$. On the other hand, the classical action can also be expressed as a function of the electron coordinates (r, θ), where the detector angle θ is determined by the detector radius r and the initial angle β. Thereafter, we have

$$S(r,\beta) = S(r,\theta(r,\beta)), \tag{32}$$

the partial derivative of which to the initial angle β gives us

$$\left(\frac{\partial S(r,\beta)}{\partial\beta}\right)_r = \left(\frac{\partial S(r,\theta)}{\partial\theta}\right)_r \left(\frac{\partial\theta(r,\beta)}{\partial\beta}\right)_r. \tag{33}$$

What is more, according to the definition of classical action,

$$dS(r,\theta) = p_r dr + L d\theta, \tag{34}$$

we get the well-known relation in analytical mechanics,

$$\left(\frac{\partial S(r,\theta)}{\partial\theta}\right)_r = L. \tag{35}$$

Since $L = kd \sin\beta$, we reach an important partial differential equation about the classical action,

$$\left(\frac{\partial S(r,\beta)}{\partial\beta}\right)_r = kd \sin\beta\left(\frac{\partial\theta}{\partial\beta}\right)_r. \tag{36}$$

After integrating the above partial differential equation over β from 0 to β_ν, we arrive at

$$S(r,\beta_\nu) = S(r,\beta = 0) + \int_0^{\beta_\nu} kd \sin\beta\left(\frac{\partial\theta}{\partial\beta}\right)_r d\beta. \tag{37}$$

Furthermore, substituting the partial derivative in Eq. (23) into the right side of the above expression, the action variation can be written out as (Appendix C)

$$\begin{aligned} S(r,\beta_\nu) = S(r,\beta = 0) + kd\Bigg(&1 - \cos\beta_\nu + \frac{1}{\xi\eta}\ln\frac{1+\gamma\cos\beta_\nu}{1+\gamma} \\ &+ \frac{1}{\xi\eta}\ln\frac{\eta^2 - \frac{d}{r} + \frac{\xi\eta}{k}p_{0r}}{\eta^2 - \frac{d}{r} + \frac{\xi\eta}{k}p_{\nu r}} - \frac{\frac{kd}{r}\sin^2\beta_\nu}{p_{0r} + p_{\nu r}}\Bigg), \end{aligned} \tag{38}$$

where

$$\gamma = \frac{2\xi\eta}{\xi^2 + \eta^2}, \tag{39}$$

and p_{0r} and $p_{\nu r}$ are the radial momentum with the initial angles $\beta = 0$ and β_ν, respectively. The action with initial angle $\beta = 0$ in Eq. (38) can be calculated easily. However, it is not needed in the following analysis and not presented here.

IV. DIFFERENTIAL CROSS SECTION

The differential cross section can be defined from the electron flux j_r crossing the spherical detector surface as [4]

$$\frac{d^2\sigma(r,\theta,\varphi)}{r^2 \sin\theta d\theta d\varphi} = \frac{2\pi E_{ph}}{c} j_r, \tag{40}$$

and

$$j_r = \mathrm{Im}(\psi^* \nabla_r \psi), \tag{41}$$

where E_{ph} and c are the photon energy and the light speed, respectively.

A. In the classically allowed region away from the caustic surface

Based on the above calculations, the electron wave arriving at the detector position (r,θ,φ), away from the classical bound

θ_m, can be constructed semiclassically as

$$\psi(r,\theta,\varphi) = \psi_{\text{out}}(R,\beta_1,\varphi)A_1 \exp\left[i\left(S_1 - \mu_1\frac{\pi}{2}\right)\right] + \psi_{\text{out}}(R,\beta_2,\varphi)A_2 \exp\left[i\left(S_2 - \mu_2\frac{\pi}{2}\right)\right]. \quad (42)$$

Substituting the expression in Eq. (1) for the outgoing wave and Eq. (42) into the electron-flux definition in Eq. (41), we have

$$j_r = \frac{k}{r^2} \times |C(k)|^2 \times \bigg\{\mathcal{A}_1^2|Y_{lm}(\beta_1,\varphi)|^2 + \mathcal{A}_2^2|Y_{lm}(\beta_2,\varphi)|^2 + \frac{p_{1r}+p_{2r}}{\sqrt{p_{1r}p_{2r}}}\mathcal{A}_1\mathcal{A}_2\text{Re}(Y_{lm}(\beta_1,\varphi)Y_{lm}^*(\beta_2,\varphi)) \times \cos\left(\Delta S - \frac{\pi}{2}\right)\bigg\}, \quad (43)$$

where Re means real part,

$$\mathcal{A}_\nu = \frac{r}{R} \times \sqrt{\frac{p_r}{k}} \times A_\nu, \quad (44)$$

and $\Delta S = S_1 - S_2$, which can be written out as (Appendix C)

$$\Delta S = kd\left(\cos\beta_2 - \cos\beta_1 + \frac{1}{\xi\eta}\ln\frac{1+\gamma\cos\beta_1}{1+\gamma\cos\beta_2} + \frac{1}{\xi\eta}\ln\frac{\eta^2 - \frac{d}{r} + \frac{\xi\eta}{k}p_{2r}}{\eta^2 - \frac{d}{r} + \frac{\xi\eta}{k}p_{1r}} + \frac{\frac{kd}{r}(\sin^2\beta_2 - \sin^2\beta_1)}{p_{1r}+p_{2r}}\right). \quad (45)$$

For numerical calculations, it is convenient to define a reduced flux,

$$\tilde{j}_r = j_r r^2 \times \frac{1}{k} \times \frac{1}{|C(k)|^2} \times \frac{1}{N_{lm}^2}, \quad (46)$$

where

$$N_{lm} = \sqrt{\frac{(2l+1)(l-m)!}{4\pi(l+m)!}}$$

is a coefficient in spherical harmonic function.

The expressions of electron flux in Eqs. (43)–(46) should be accurate in the classically allowed region not too close to the caustic (where $\Delta S \gtrsim \pi$). [As usual when calculating differential cross sections, the gradient in Eq. (41) acts on both the phase and on the amplitudes A_ν; the latter fall off as r^{-1} giving a term which is proportional to r^{-2}, which is negligible at large r, and which is ignored.] Formulas for the detached electron flux on a planar detector are presented in Appendix D.

B. Near the caustic surface and extending to the classically forbidden region

Near the caustic surface, the flux expressed in Eq. (46) diverges, and a corrected approximation is needed. The caustic surface is *a fold catastrophe*, where the wave function can be approximated by an Airy function [15]. Such approximation gives a finite result at the caustic surface, and a result which, when ΔS is large, approaches that in Eq. (46).

The usual way to obtain this corrected approximation is to convert the wave function to an Airy-function form. We use a somewhat different but similar approach, converting the differential cross section to an Airy-function form. To be clear, we take an s-wave source, for example.

First, Eq. (46) gives the behavior of the electron flux at large ΔS,

$$\tilde{j}_r = \mathcal{A}_1^2 + \mathcal{A}_2^2 + 2P_{\text{ratio}}\mathcal{A}_1\mathcal{A}_2\cos\left(\Delta S - \frac{\pi}{2}\right). \quad (47)$$

where,

$$P_{\text{ratio}} = \frac{p_{1r}+p_{2r}}{2\sqrt{p_{1r}p_{2r}}}. \quad (48)$$

The expression in Eq. (47) can be separated as

$$\tilde{j}_r = (\mathcal{A}_1^2 + \mathcal{A}_2^2 + 2P_{\text{ratio}}\mathcal{A}_1\mathcal{A}_2)\sin^2\left(\frac{\Delta S}{2} + \frac{\pi}{4}\right) + (\mathcal{A}_1^2 + \mathcal{A}_2^2 - 2P_{\text{ratio}}\mathcal{A}_1\mathcal{A}_2)\cos^2\left(\frac{\Delta S}{2} + \frac{\pi}{4}\right). \quad (49)$$

Note that the asymptotic behavior of Airy function $\text{Ai}(\zeta)$ at negative large ζ is just such a form as the first factor on the right side of the above expression,

$$\text{Ai}(\zeta) \doteq \frac{1}{\sqrt{\pi}|\zeta|^{\frac{1}{4}}}\sin\left(\frac{2}{3}|\zeta|^{\frac{3}{2}} + \frac{\pi}{4}\right), \quad \zeta \text{ is negative large}, \quad (50)$$

and also,

$$\text{Ai}'(\zeta) \doteq -\frac{|\zeta|^{\frac{1}{4}}}{\sqrt{\pi}}\cos\left(\frac{2}{3}|\zeta|^{\frac{3}{2}} + \frac{\pi}{4}\right), \quad \zeta \text{ is negative large}, \quad (51)$$

is the same form as the second part on the right side of the above expression. Therefore, the expression Eq. (49) can be replaced by

$$\tilde{j}_r = \left[\pi|\zeta|^{\frac{1}{2}}(\mathcal{A}_1^2 + \mathcal{A}_2^2 + 2P_{\text{ratio}}\mathcal{A}_1\mathcal{A}_2)\right] \times \text{Ai}^2(\zeta) + \left[\pi|\zeta|^{-\frac{1}{2}}(\mathcal{A}_1^2 + \mathcal{A}_2^2 - 2P_{\text{ratio}}\mathcal{A}_1\mathcal{A}_2)\right] \times \text{Ai}'^2(\zeta), \quad (52)$$

where

$$\zeta = -\left(\tfrac{3}{4}\Delta S\right)^{2/3}, \quad \theta < \theta_m. \quad (53)$$

Equation (52) can be used directly in the classically allowed region $\theta \in [0,\theta_m)$ to calculate electron flux.

As the detection angle θ approaches the classical allowed boundary θ_m on the spherical detector, the flux expressed in the formula in Eq. (52) will converge to a finite value, noting

$$\mathcal{A}_1^2(\Delta S)^{1/3} \to \frac{\sin\beta_1}{\sin\theta}\left\{\frac{-2kd\cos\beta_1}{3\left[\left(\frac{\partial^2\theta}{\partial\beta_1^2}\right)_r\right]^2}\right\}^{1/3}, \quad \theta \to \theta_m, \quad (54)$$

where

$$\left[\left(\frac{\partial^2\theta}{\partial\beta_1^2}\right)_r\right]_{\theta=\theta_m} = \frac{\Pi - \Lambda}{\varepsilon^2}, \quad (55)$$

and

$$\Pi = 2\xi^2\eta^2\sin\beta_1\cos\beta_1\left(1 - \frac{kd}{rp_{1r}}\cos\beta_1\right); \quad (56)$$

$$\Lambda = \frac{k}{p_{1r}}\sin\beta_1\left(1 - \frac{k^2d^2}{r^2p_{1r}^2}\cos^2\beta_1\right)\left[\eta^2 - \frac{d}{r}(1+\varepsilon^2)\right]. \quad (57)$$

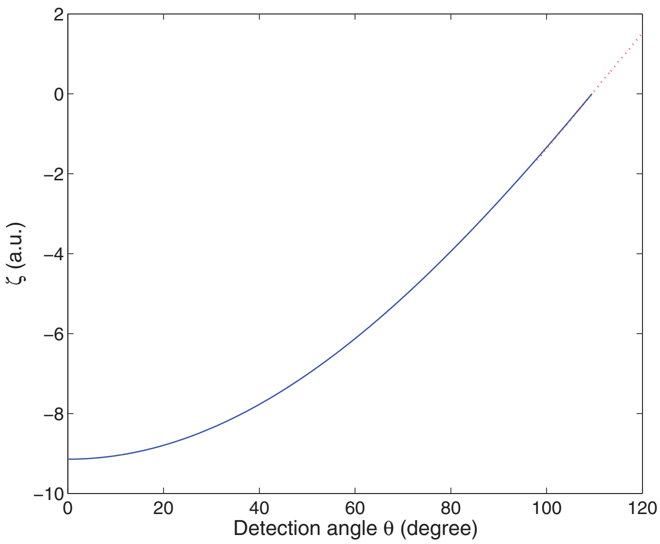

FIG. 4. (Color online) Linear approximation for the argument of the Airy function near the caustic, where the following parameters are used: $d = 300a_0$, $\alpha = 1$, $\widetilde{E} = 2$, and $r \gg d$. The argument in the classically allowed region, $\zeta = -(\frac{3}{4}\Delta S)^{2/3}$, is given by the blue solid curve, and the linear approximation near the caustic is displayed by the red dotted line.

In the classically forbidden region, the electron flux can be obtained by extending the flux in Eq. (52) in the classically allowed region. One can expand both the prefactors and the argument of the Airy functions as a power series of $(\theta - \theta_m)$ near the caustic surface to get approximations. Here, we find the linear approximation for the argument of Airy functions is sufficient, that is,

$$\zeta = 2^{1/3}k^{2/3}d^{2/3}\left[\frac{\cos^2\beta_1}{-\left(\frac{\partial^2\theta}{\partial\beta_1^2}\right)_r}\right]^{1/3}_{\theta=\theta_m}(\theta-\theta_m), \quad \theta \geqslant \theta_m. \tag{58}$$

Figure 4 demonstrates the approximation near the caustic. The linear approximations for the quantities in the square brackets before the Airy functions in Eq. (52) can be obtained conveniently by numerically applying the least square procedure inside the classically allowed region which should not be too far away from the boundary θ_m to ensure accuracy.

For other wave sources and laser polarization, the flux can also be obtained following the above procedure. Taking a p-wave source and the linearly polarized laser along the z axis, the flux can be obtained as

$$\begin{aligned}\widetilde{j}_r &= \left[\pi|\zeta|^{\frac{1}{2}}\left(\mathcal{B}_1^2+\mathcal{B}_2^2+2P_{\text{ratio}}\mathcal{B}_1\mathcal{B}_2\right)\right]\times \mathrm{Ai}^2(\zeta)\\ &\quad+\left[\pi|\zeta|^{-\frac{1}{2}}\left(\mathcal{B}_1^2+\mathcal{B}_2^2-2P_{\text{ratio}}\mathcal{B}_1\mathcal{B}_2\right)\right]\times \mathrm{Ai}'^2(\zeta),\end{aligned} \tag{59}$$

where $\mathcal{B}_1 = \mathcal{A}_1\cos\beta_1$ and $\mathcal{B}_2 = \mathcal{A}_2\cos\beta_2$. The flux can also be extended into the classically forbidden region in a similar way.

C. Asymptotic behavior

The above formulas have been presented for any spherical detector with a finite radius r. When the spherical detector is far away, that is, $r \gg d$, these expressions can be simplified greatly. Here, we present some useful quantities.

First, the cross-over angle θ_c can be simplified as

$$\theta_c = \arccos\left(\frac{1}{1+2\widetilde{E}}\right), \tag{60}$$

and the classically allowed maximum angle θ_m on the detector can be written as

$$\theta_m = \arccos\left(\frac{1-\widetilde{E}}{1+\widetilde{E}}\right). \tag{61}$$

Second, the partial derivative of the detector angle with respect to the initial angle can be simplified as

$$\left(\frac{\partial\theta}{\partial\beta}\right)_r = 1 - \frac{1}{\xi\eta}\times\frac{\gamma}{1+\gamma\cos\beta}, \tag{62}$$

and

$$\left(\frac{\partial^2\theta}{\partial\beta^2}\right)_r = -\frac{1}{\xi\eta}\times\frac{\gamma^2\sin\beta}{(1+\gamma\cos\beta)^2}. \tag{63}$$

Third, the action difference becomes

$$\Delta S = kd\left(\cos\beta_2 - \cos\beta_1 + \frac{1}{\xi\eta}\ln\frac{1+\gamma\cos\beta_1}{1+\gamma\cos\beta_2}\right). \tag{64}$$

Finally, the flux expression can also be simplified. Specifically for the s-wave source, we have

$$\widetilde{j}_r = \pi\times\left[(\mathcal{A}_1+\mathcal{A}_2)^2|\zeta|^{\frac{1}{2}}\times \mathrm{Ai}^2(\zeta) + \frac{(\mathcal{A}_1-\mathcal{A}_2)^2}{|\zeta|^{\frac{1}{2}}}\times \mathrm{Ai}'^2(\zeta)\right]. \tag{65}$$

And for the p_z-wave source and the linear polarized laser along the z axis, we also have

$$\widetilde{j}_r = \pi\times\left[(\mathcal{B}_1+\mathcal{B}_2)^2|\zeta|^{\frac{1}{2}}\times \mathrm{Ai}^2(\zeta) + \frac{(\mathcal{B}_1-\mathcal{B}_2)^2}{|\zeta|^{\frac{1}{2}}}\times \mathrm{Ai}'^2(\zeta)\right]. \tag{66}$$

V. CALCULATIONS AND DISCUSSIONS

We now calculate and discuss the detached-electron flux using the above formulas. In Fig. 5, we display the spatial variations of detached-electron flux for both an s-wave source and a p_z-wave source corresponding to the trajectory patterns in Fig. 2 and analyzed previously in Sec. II. One can see that the caustic surfaces always correspond to enhanced quantum flux distributions. In the following, we discuss several specific physical effects.

A. Effects of the observing distance from the force center

We first examine an s-wave source such as in the photodetachment of S$^-$. Some results for different distances are displayed in Fig. 6. For this s-wave source, alternative calculations indicated by dots based on the exact Coulomb Green's function (Appendix E) confirm the accuracy of the present method, and meanwhile exhibit the following merits of our present semiclassical calculation. The semiclassical calculation turns out to be much faster than the calculation based on the exact Coulomb Green's function, which proved

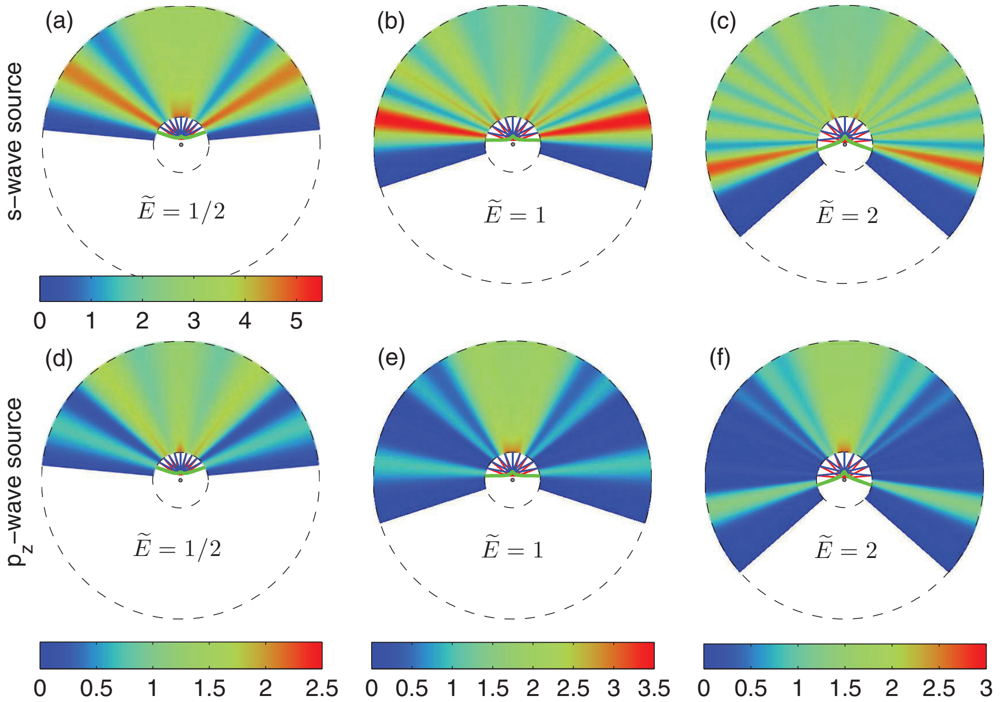

FIG. 5. (Color online) Spatial distributions of the quantum flux plotted from $r = 1000a_0$ to $r = 5000a_0$ with the corresponding trajectory patterns shown in the regions $r < 1000a_0$. Here $d = 300a_0$ and $\alpha = 1$. (a)–(c) are for an s-wave source and (d)–(f) for a p_z wave. Note for $\widetilde{E} = 1/2$, different color bars are used for an s-wave source and for a p_z-wave source.

to be time-consuming as a result of the Whittaker function of the second kind. Besides that, the definition of the Green's function implicitly involves a spherically symmetric source; treatment of other sources is not available to our knowledge. In contrast, the present semiclassical approach and its resulting expressions are valid for s waves or any other sources. Most important, a very clear physical picture is obtained from the semiclassical analysis, which the exact Green's function does not provide.

Let us examine the dependence of the differential cross section on the radius r of the spherical detector centered at the force center. We observe that in Fig. 6 the greatest change is near $\theta \approx 0$ (backward-scattered electrons). There is a large current near the positive z axis at small r, but it drops off rapidly at large r. We see also with increasing r a shift in the boundary of the classically allowed region from about 90° to 110°, and with it a shift in the interference pattern. However, the number of peaks is unchanged. It is determined by the classical action S_{COT} along a closed orbit lying on the z axis going from the source to the classical turning point and back to the source,

$$S_{\text{COT}} = kd\left(2 + \frac{1}{\xi\eta}\ln\frac{1-\gamma}{1+\gamma}\right), \tag{67}$$

obtained from Eq. (45) or Eq. (64), which is independent of the detector distance r.

For a p_z-wave source, similar effects on the observing distance are displayed in Fig. 7 but now the detached-electron flux is considerably reduced near the center of the observing angles.

B. Effect of scaled energy

Differential cross sections at three different scaled energies are shown in Fig. 8. The boundary of the allowed region for each case is marked by a dashed line. We see that as the scaled energy increases, the allowed region increases, crossing 90° when $\widetilde{E} = 1$. The boundary of that region is close to an inflection point in the graph of the differential cross section, where the behavior changes from oscillatory in the allowed region to decaying exponential in the forbidden region. Also, as $\widetilde{E}$ increases, the number of interference peaks in the differential cross section increases.

C. Effect of the angular distribution of outgoing waves

For a p_z-wave source, the outgoing wave has a node at $\beta = \pi/2$. This means that the trajectory going out at that angle has zero amplitude. At the corresponding point θ_c in the differential cross section, only one term contributes. These points are marked as dotted lines in Fig. 8. The effect of the node is greater at large scaled energy (Fig. 9). There, the cross-over angle θ_c tend to $\pi/2$ and the flux profile gives the p-wave spatial structure more clearly.

D. Effect of the distance between the source and the force center

The classical differential cross section for large r depends only on the scaled energy $\widetilde{E} = Ed/\alpha$, so the distance between the ion and the force center has the same effect as the energy. However, when we include the interference effects, the distance has a large effect. According to Eq. (45), the

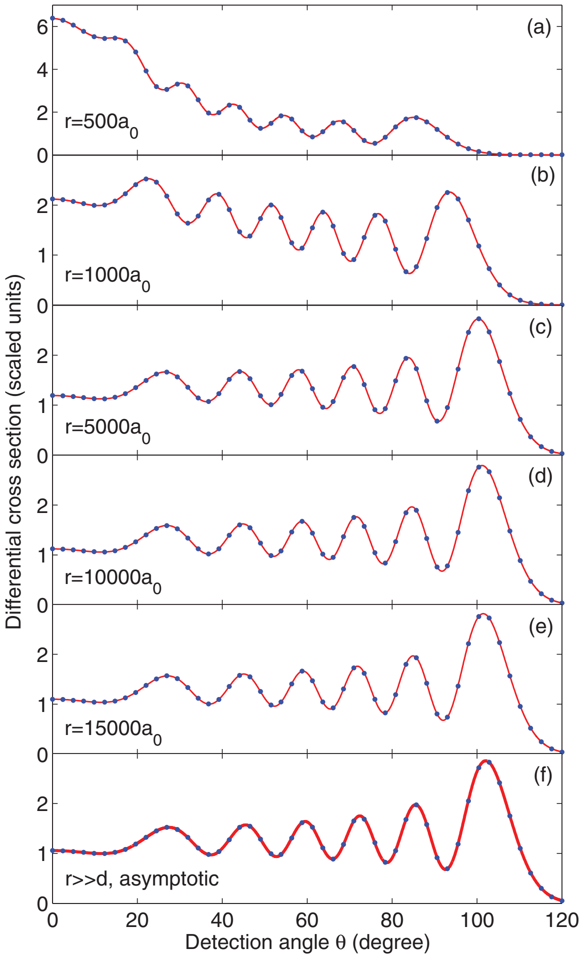

FIG. 6. (Color online) Calculated differential cross sections on spherical screens at different detection distances for an s-wave source. Here $d = 300a_0$, $\alpha = 1$, and $\widetilde{E} = 2$. The results from our semiclassical propagation approach are displayed as solid curves. They are compared with the results from the exact Coulomb Green's function method (dots). The agreement between the two independent approaches indicates that results from both approaches are correct.

action difference between the two interfering trajectories is proportional to d. Therefore, as d increases, the number of oscillations in the interference pattern also increases.

E. Dependence of the electron flux on the model parameters

The dependence of the interference structure on the other parameters, such as the electron energy E, the distance d between the wave source and the force center, and the negative-charge number α at the force center, is also very interesting. Generally, with all the parameters increasing, the number of interference rings also increases, but the details are different.

Here, we display the dependence of the differential cross sections on the distance d between the wave source and the force center (Fig. 10). As d is increased, the position θ_c and the electron-signal range θ_m are almost fixed for large r. Actually, for large r, the envelop of the differential cross sections hardly changes but the number of oscillations in the envelop increases significantly. One can understand this point from the scaling property in the system.

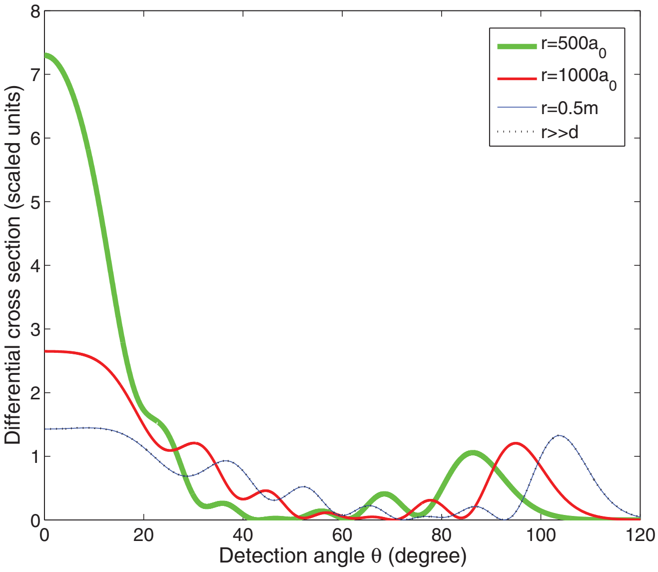

FIG. 7. (Color online) Differential cross sections for a p-wave source on spherical detectors at different distances, here $d = 300a_0$, $\alpha = 1$, and $\widetilde{E} = 2$. The green, red, and blue curves are calculated, respectively, at $r = 500a_0$, $r = 1000a_0$, and $r = 0.5m$. Note the asymptotic behavior for $r \gg d$ denoted by the dotted line is hardly distinguishable from the one at $r = 0.5m$.

F. Scaling spectroscopy

Going through the analytical formulas presented in the previous sections, one can verify that the differential cross

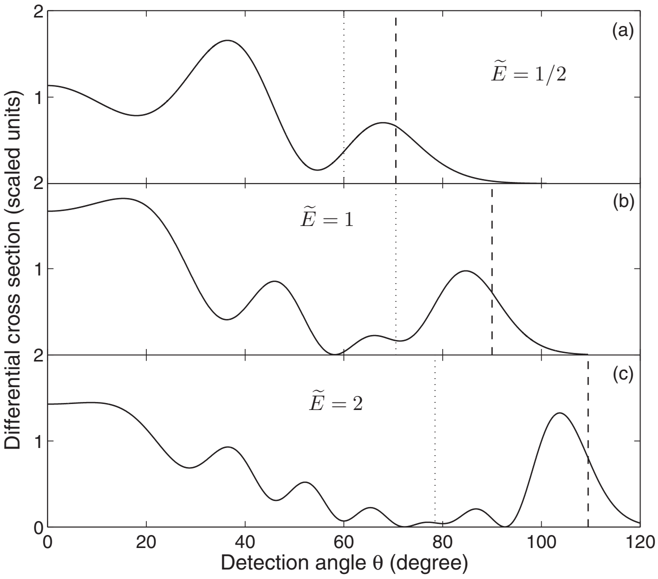

FIG. 8. Differential cross sections observed on spherical detectors at very large distances $r \gg d$ for a p_z-wave source. The three curves correspond to the three typical trajectory patterns in Fig. 2. Here $d = 300a_0$ and $\alpha = 1$. The cross-over angle θ_c and the classically allowed boundary θ_m on the spherical screen are indicated by the dotted lines and the dashed lines.

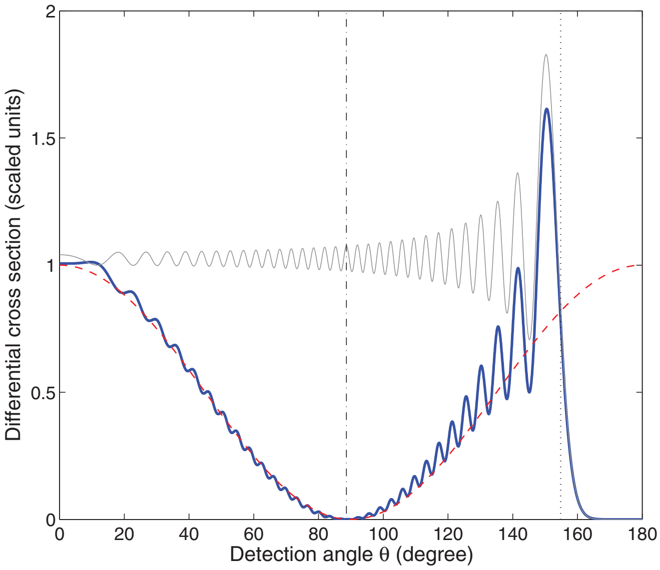

FIG. 9. (Color online) The angular distribution of outgoing waves from the source dramatically affects the differential cross section at high energy. Here we compare the differential cross sections of a p-wave source (blue and thick) and of an s-wave source (black and thin). Here $\widetilde{E} = 20$, $d = 300a_0$, $\alpha = 1$, and $r \gg d$. The dashed curve (red) depicts the spatial structure ($\cos^2\theta$) of the p-wave source itself. The dot-dashed line and the dotted one indicate the position of θ_c and θ_m, respectively.

section is completely determined by the following three scaled parameters: $\widetilde{E} = Ed/\alpha$, $\tilde{r} = r/d$, and $\omega = kd$, not dependent on α, d, E, and r separately. The scaled Hamiltonian can be written as

$$h = \frac{\widetilde{p_r}^2}{2} + \frac{\widetilde{L}^2}{2\tilde{r}^2} + \frac{1}{\tilde{r}} - 1, \tag{68}$$

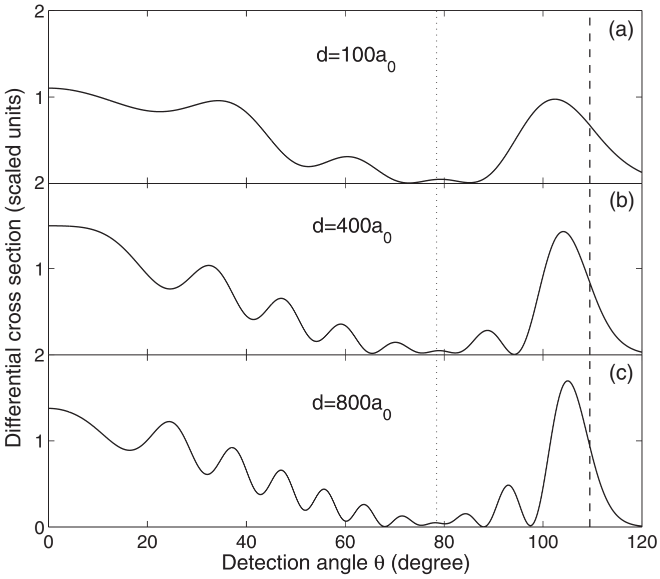

FIG. 10. Differential cross sections (solid lines) for a p-wave source with different distances d between the wave source and the repulsive force center. Here $\alpha = 1$, $\widetilde{E} = 2$, and $r \gg d$. The dotted line and the dashed one indicate the position of θ_c and θ_m, respectively.

where

$$\widetilde{L} = \tilde{k}\tilde{d}\sin\beta,$$

with $\tilde{k} = \sqrt{2\widetilde{E}}$, $\tilde{d} = 1$ and $\tilde{\alpha} = 1$.

If the four model parameters, including the negative-charge number α in the force center, the distance between the wave source and the force center d, electron energy E, and the detector location r relative to the force center, satisfy the scaling relations $\widetilde{E} = Ed/\alpha$ and $\tilde{r} = r/d$, the scaled classical trajectory pattern is unchanged, such as the patterns displayed in Fig. 2. As a direct result, for large r, the envelop for the oscillating differential cross section on the spherical detector does not change as illustrated in Fig. 10.

G. Comparison with the photodetachment in a homogeneous electric field

It is beneficial to compare the present system with the photodetachment of negative ion in a homogeneous electric field [4]. Here, we discuss some important differences and similarities between the two systems.

As we have shown in the previous sections, in the present system, the electron flux at dark-ring positions is not zero. This is because the amplitudes A_1 and A_2 corresponding to the two interference trajectories are quite different in value. This is true even when the spherical detector is far away from the force center. However, in a uniform electric field, when the plane detector is located sufficiently away, the initial angles for the two interference trajectories are approximately symmetric relative to $\pi/2$, and the amplitudes are almost equal. This leads to the zero-flux dark rings for detachment in an electric field when the observation plane is far away from the ion.

One advantage of the present system is the clear separation and manipulation of θ_c and θ_m appearing in the differential cross sections. This makes it feasible to observe the quantum wave-source angular structure in photodetachment microscopy experiments [5]. In contrast, in a uniform electric field, large separation of θ_c and θ_m is difficult to achieve.

We note that in the limit of low scaled energy $\widetilde{E}$, the potential function in Eq. (2) acting on the detached electron near the wave source can be approximated as

$$V(r) = \frac{\alpha}{r} - \frac{\alpha}{d} \approx -\frac{\alpha}{d^2}(z - z_{\text{ion}}),$$

where z_{ion} is the z coordinate of the negative ion relative to the force center. Therefore, in the limit of low scaled energy the dynamics of the present system near the wave source resembles that in a uniform electric field with an effective field α/d^2.

VI. CONCLUSIONS

Inspired by an experiment of the Washington group [1] and based on our previous studies on the photodetachment of negative ion in an external field, we constructed a theoretical model of the scattering of a point wave source near a repulsive-force center. Completely analytical results for the classical trajectory and the quantum differential cross section have been presented in this paper.

For the classical motion, three typical trajectory patterns were obtained, which correspond to the scaled energy smaller than, equal to, or larger than unity (Fig. 2). To obtain the semiclassical differential cross section, two problems have been solved: first, the reduced semiclassical amplitude was obtained, whose physical interpretation was given and illustrated; second, the flux expression, for the classically accessible region, was obtained, and then was extended to the classically forbidden region. The accuracy of the semiclassical propagation method is shown to be excellent through comparison with an exact Coulomb Green's function for an s-wave source.

Finally, we have demonstrated and discussed some interesting phenomena occurring in the present system. They include the interference patterns on the spherical detector corresponding to the three cases and their dependencies on the parameters, the scaling property of the differential cross sections, and the comparison with photodetachment in a uniform electric field.

ACKNOWLEDGMENTS

B.C.Y. and M.L.D. acknowledge the support from NSFC Grants No. 11074260 and No. 11121403. J.B.D. acknowledges support from NSF Grant No. 1068344.

APPENDIX A: THE DERIVATION OF EQ. (8) AND EQS. (13)–(16)

First we set

$$\tilde{x} = 2\widetilde{E}\sin^2(\beta).$$

Then, from the orbit equation Eq. (5), we have

$$[(d - r\cos\theta)^2 + r^2\sin^2(\theta)]\tilde{x}^2 + [2r(1-\cos\theta)(d - r\cos\theta) - 2\widetilde{E}r^2\sin^2(\theta)]\tilde{x} + r^2(1-\cos\theta)^2 = 0. \tag{A1}$$

The discriminant for the existence of real root x can be calculated as

$$\Delta = 4r^4\sin^2(\theta)(1-\cos\theta) \times \left[(\widetilde{E}+1)^2\cos(\theta) + \widetilde{E}^2 - 1 - 2\widetilde{E}\frac{d}{r}\right] \geqslant 0, \tag{A2}$$

which gives us

$$\delta = (\widetilde{E}+1)^2\cos(\theta) + \widetilde{E}^2 - 1 - 2\widetilde{E}\frac{d}{r} \geqslant 0. \tag{A3}$$

Using the maximum θ expression in Eq. (11), we can write δ as

$$\delta = (\widetilde{E}+1)^2(\cos\theta - \cos\theta_m). \tag{A4}$$

Furthermore, we can get the solution $\tilde{x}$ from Eqs. (A1)–(A4) as

$$\tilde{x}_{1,2} = (1-\cos\theta)(\widetilde{E}+1) \times \frac{(1+\cos\theta) - \frac{1+\frac{d}{r}}{\widetilde{E}+1} \pm \sqrt{(1+\cos\theta)(\cos\theta - \cos\theta_m)}}{\left(1-\frac{d}{r}\right)^2 + 2\frac{d}{r}(1-\cos\theta)}. \tag{A5}$$

For convenience, we define

$$\tilde{a} = (1+\cos\theta)/2; \tag{A6}$$

$$\tilde{b} = (\cos\theta - \cos\theta_m)/2. \tag{A7}$$

Then,

$$(1+\cos\theta) - \frac{1+\frac{d}{r}}{\widetilde{E}+1} = \tilde{a} + \tilde{b} - \frac{1}{(\widetilde{E}+1)^2}\cdot\frac{d}{r}; \tag{A8}$$

$$\sqrt{(1+\cos\theta)(\cos\theta - \cos\theta_m)} = 2\sqrt{\tilde{a}\tilde{b}}. \tag{A9}$$

In addition, we have

$$1 - \cos\theta_c = \frac{2\widetilde{E}}{2\widetilde{E}+1}\left(1 - \frac{d}{r}\right). \tag{A10}$$

Substituting Eqs. (A8)–(A10) in Eq. (A5), we have $\tilde{x}_{1,2} = 2\widetilde{E}x_{1,2}$, and

$$x_{1,2} = (1-\cos\theta) \times \frac{\frac{\widetilde{E}+1}{2}\left(\sqrt{1+\cos\theta} \pm \sqrt{\cos\theta - \cos\theta_m}\right)^2 - \frac{1}{\widetilde{E}+1}\frac{d}{r}}{(2\widetilde{E}+1)\left(1-\frac{d}{r}\right)(1-\cos\theta_c) + 4\widetilde{E}\frac{d}{r}(1-\cos\theta)}, \tag{A11}$$

which gives us the value of $\sin\beta_{1,2} = \sqrt{x_{1,2}}$.

After a brief analysis, one finds these trajectories touching the caustic correspond to the larger value of $\sin\beta$ with an obtuse angle β. The initial angle β for another trajectory also becomes greater than $\pi/2$ as the observing spherical angle θ increases and crosses over the critical angle θ_c.

APPENDIX B: REDUCTION OF THE JACOBIAN IN EQ. (21)

Here we present the details going from the two-dimensional Jacobian in Eq. (21) to the simpler expression in Eq. (22). The present reduction can be considered as the continuation of an Appendix of [10]. First, the motion equation can be formally written as

$$r = r(t,\beta); \tag{B1}$$

$$\theta = \theta(t,\beta), \tag{B2}$$

from which, if the distance r is fixed as a constant, we have the following two relations:

$$\left(\frac{\partial r}{\partial\beta}\right)_t = -\left(\frac{\partial r}{\partial t}\right)_\beta\left(\frac{\partial t}{\partial\beta}\right)_r; \tag{B3}$$

$$\left(\frac{\partial\theta}{\partial\beta}\right)_t = \left(\frac{\partial\theta}{\partial\beta}\right)_r - \left(\frac{\partial\theta}{\partial t}\right)_\beta\left(\frac{\partial t}{\partial\beta}\right)_r. \tag{B4}$$

On the other hand, the orbit equation can be formally written as

$$r = r[\theta(t,\beta)], \tag{B5}$$

from which we have

$$\left(\frac{\partial r}{\partial\beta}\right)_t = \frac{dr}{d\theta}\left(\frac{\partial\theta}{\partial\beta}\right)_t. \tag{B6}$$

Now eliminate the partial derivative $(\frac{\partial t}{\partial\beta})_r$ in Eq. (B4) using the relations in Eqs. (B3) and (B6), we get

$$\left(\frac{\partial\theta}{\partial\beta}\right)_t = \frac{\left(\frac{\partial r}{\partial t}\right)_\beta}{\left(\frac{\partial r}{\partial t}\right)_\beta - \frac{dr}{d\theta}\cdot\left(\frac{\partial\theta}{\partial t}\right)_\beta}\left(\frac{\partial\theta}{\partial\beta}\right)_r. \tag{B7}$$

After substituting the expressions in Eqs. (B6) and (B7) into the two-dimensional determinant in Eq. (21), we have

$$\det\left(\frac{\partial(r,\theta)}{\partial(t,\beta_\nu)}\right) = p_r\left(\frac{\partial\theta}{\partial\beta_\nu}\right)_r. \tag{B8}$$

APPENDIX C: THE DERIVATION OF EQS. (23) AND (38)

From Eq. (10), we have

$$\theta = \theta_0 + \theta_p, \tag{C1}$$

where

$$\theta_p = \arccos\left(\frac{1+\frac{d}{r}\xi^2\sin^2(\beta)}{\varepsilon}\right). \tag{C2}$$

According to Eq. (7),

$$\cos\theta_0 = \frac{1+\xi^2\sin^2\beta}{\varepsilon}; \tag{C3}$$

$$\sin\theta_0 = -\frac{\xi^2\sin\beta\cos\beta}{\varepsilon}, \tag{C4}$$

we obtain

$$\left(\frac{\partial\cos\theta_0}{\partial\beta}\right)_r = \frac{\xi^2\sin\beta\cos\beta}{\varepsilon}\left(1+\frac{1-\eta^2}{\varepsilon^2}\right). \tag{C5}$$

Thus,

$$\left(\frac{\partial\theta_0}{\partial\beta}\right)_r = 1+\frac{1-\eta^2}{\varepsilon^2}. \tag{C6}$$

According to Eq. (C2),

$$\cos\theta_p = \frac{1+\frac{d}{r}\xi^2\sin^2\beta}{\varepsilon}; \tag{C7}$$

$$\sin\theta_p = \frac{\xi\sin\beta}{\varepsilon}\times\sqrt{\eta^2-2\frac{d}{r}-\frac{d^2}{r^2}\xi^2\sin^2\beta}, \tag{C8}$$

we obtain

$$\left(\frac{\partial\cos\theta_p}{\partial\beta}\right)_r = -\frac{\xi^2\sin\beta\cos\beta}{\varepsilon}\times\frac{\eta^2-\frac{d}{r}(1+\varepsilon^2)}{\varepsilon^2}. \tag{C9}$$

Using Eq. (C8) and the following relationship,

$$\sqrt{\eta^2-2\frac{d}{r}-\frac{d^2}{r^2}\xi^2\sin^2\beta} = \frac{p_r}{k}\times\xi, \tag{C10}$$

we have

$$\left(\frac{\partial\theta_p}{\partial\beta}\right)_r = \frac{\eta^2-\frac{d}{r}(1+\varepsilon^2)}{\varepsilon^2}\times\frac{k}{p_r}\cos\beta. \tag{C11}$$

Combining Eqs. (C6) and (C11), we arrive at

$$\left(\frac{\partial\theta}{\partial\beta}\right)_r = 1+\frac{1-\eta^2}{\varepsilon^2}+\frac{\eta^2-\frac{d}{r}(1+\varepsilon^2)}{\varepsilon^2}\times\frac{k}{p_r}\cos\beta. \tag{C12}$$

We denote the action difference $S(r,\beta_\nu)-S(r,\beta=0)$ as S_d, then from Eq. (37),

$$S_d = \int_0^{\beta_\nu} kd\sin\beta\left(\frac{\partial\theta}{\partial\beta}\right)_r d\beta. \tag{C13}$$

Using Eq. (C12), the above S_d can be written out completely as

$$\begin{aligned} S_d = kd\times\Bigg[&(1-\cos\beta_\nu)+(1-\eta^2)\Gamma \\ &+\xi\left(\eta^2-\frac{d}{r}\right)\Omega-\xi\times\frac{d}{r}\times\Xi\Bigg], \end{aligned} \tag{C14}$$

where

$$\Gamma = \int_0^{\beta_\nu}\frac{\sin\beta}{1+\xi^2\eta^2\sin^2\beta}d\beta; \tag{C15}$$

$$\Xi = \int_0^{\beta_\nu}\frac{\sin\beta\cos\beta}{\sqrt{\eta^2-2\frac{d}{r}-\frac{d^2}{r^2}\xi^2\sin^2\beta}}d\beta; \tag{C16}$$

$$\Omega = \int_0^{\beta_\nu}\frac{\sin\beta\cos\beta}{(1+\xi^2\eta^2\sin^2\beta)\times\sqrt{\eta^2-2\frac{d}{r}-\frac{d^2}{r^2}\xi^2\sin^2\beta}}d\beta. \tag{C17}$$

The Γ and Ξ can be integrated straightforward as

$$\Gamma = -\frac{1}{\sqrt{1+\xi^2\eta^2}}\times\frac{1}{2\xi\eta}\times\ln\left(\frac{1+\gamma\cos\beta_\nu}{1-\gamma\cos\beta_\nu}\times\frac{1-\gamma}{1+\gamma}\right); \tag{C18}$$

$$\Xi = \frac{\sin^2\beta_\nu}{\sqrt{\eta^2-2\frac{d}{r}-\frac{d^2}{r^2}\xi^2\sin^2\beta_\nu}+\sqrt{\eta^2-2\frac{d}{r}}}. \tag{C19}$$

Using the following relationships in order,

$$1-\eta^2 = -\sqrt{1+\xi^2\eta^2}; \tag{C20}$$

$$1-\gamma^2\cos\beta_\nu = \frac{\varepsilon^2}{1+\xi^2\eta^2}; \tag{C21}$$

$$1+\xi^2\eta^2 = \frac{1}{1-\gamma^2}, \tag{C22}$$

Γ can be written as

$$\Gamma = \frac{1}{1-\eta^2}\times\frac{1}{\xi\eta}\times\left[-\ln\varepsilon+\ln\frac{1+\gamma\cos\beta_\nu}{1+\gamma}\right]. \tag{C23}$$

Using the relationship Eq. (C10), Ξ can also be written as

$$\Xi = \frac{k}{\xi}\times\frac{\sin^2\beta}{p_{0r}+p_{\nu r}}. \tag{C24}$$

Replacing the variable β by

$$y(\beta) = \sqrt{\eta^2-2\frac{d}{r}-\frac{d^2}{r^2}\xi^2\sin^2\beta}, \tag{C25}$$

then Ω can be calculated as

$$\Omega = \frac{1}{2(\eta^2-\frac{d}{r})\xi^2\eta}\times\left[\ln\frac{\eta^2-\frac{d}{r}-\eta y(\beta)}{\eta^2-\frac{d}{r}+\eta y(\beta)}\right]_0^{\beta_\nu}. \tag{C26}$$

Substituting the expression $y(\beta)$ into the above equation, we have

$$\begin{aligned} \Omega = {}&\frac{1}{(\eta^2-\frac{d}{r})\xi^2\eta} \\ &\times\left[\ln\varepsilon+\ln\frac{\eta^2-\frac{d}{r}+\eta\sqrt{\eta^2-2\frac{d}{r}}}{\eta^2-\frac{d}{r}+\eta\sqrt{\eta^2-2\frac{d}{r}-\frac{d^2}{r^2}\xi^2\sin^2\beta_\nu}}\right]. \end{aligned} \tag{C27}$$

Using the relationship in Eq. (C10), we arrive at

$$\Omega = \frac{1}{(\eta^2 - \frac{d}{r})\xi^2\eta} \times \left[\ln\varepsilon + \ln\frac{\eta^2 - \frac{d}{r} + \frac{\xi\eta}{k}p_{0r}}{\eta^2 - \frac{d}{r} + \frac{\xi\eta}{k}p_{\nu r}} \right]. \tag{C28}$$

Equation (38) is obtained by substituting Eqs. (C23), (C24), and (C28) into Eq. (C14).

APPENDIX D: SPATIAL INTERFERENCE ON A PLANE SCREEN

Here, we present some useful formulas for the spatial interference pattern on a plane detector perpendicular to the z axis. Similar to the formula in Eq. (43) for the flux on a spherical detector, the spatial interference pattern on a plane detector, which intersects the z axis at $z > d$, has the following "primitive" form in the classically allowed region,

$$\begin{aligned} j_z = \frac{k}{r^2} \times |C(k)|^2 \times \Bigg\{ & \frac{p_{1z}}{p_{1r}}\mathcal{A}_1^2|Y_{lm}(\beta_1,\varphi)|^2 \\ & + \frac{p_{2z}}{p_{2r}}\mathcal{A}_2^2|Y_{lm}(\beta_2,\varphi)|^2 \\ & + \frac{p_{1z}+p_{2z}}{\sqrt{p_{1r}p_{2r}}}\mathcal{A}_1\mathcal{A}_2\mathrm{Re}(Y_{lm}(\beta_1,\varphi)Y_{lm}^*(\beta_2,\varphi)) \\ & \times \cos\left(\Delta S - \frac{\pi}{2}\right)\Bigg\}, \end{aligned} \tag{D1}$$

where

$$p_{\nu z} = p_{\nu r}\cos\theta - \frac{kd}{r}\sin\beta\sin\theta, \tag{D2}$$

and Re means real part.

For scaled energy $\widetilde{E} \geqslant 1$, the above flux expression can be used everywhere on the plane detector due to the absence of the caustic surface on the plane detector. For scaled energy less than a unity, a classical boundary will be found at

$$\begin{aligned} \rho_m &= \frac{2\sqrt{\widetilde{E}}}{1-\widetilde{E}^2} \times \sqrt{[(\widetilde{E}+1)z - \widetilde{E}d][(\widetilde{E}+1)z - d]}, \\ & 0 < \widetilde{E} < 1, \end{aligned} \tag{D3}$$

which is from the caustic surface in Eq. (9) and has the following asymptotic form,

$$\rho_m = z \times \frac{2\sqrt{\widetilde{E}}}{1-\widetilde{E}}, \tag{D4}$$

for $z \gg d$. Near the boundary between classically allowed and forbidden regions, the above semiclassical formula can be extended to the forbidden region using the Airy function in a similar way. Similar to Eq. (46), the reduced flux on the plane can be defined as

$$\widetilde{j}_z = j_z z^2 \times \frac{1}{k} \times \frac{1}{|C(k)|^2} \times \frac{1}{N_{lm}^2}, \tag{D5}$$

then

$$\begin{aligned} \widetilde{j}_z = \frac{z^2}{r^2} \times \frac{1}{N_{lm}^2} \times \Bigg\{ & \frac{p_{1z}}{p_{1r}}\mathcal{A}_1^2|Y_{lm}(\beta_1,\phi)|^2 \\ & + \frac{p_{2z}}{p_{2r}}\mathcal{A}_2^2|Y_{lm}(\beta_2,\phi)|^2 \\ & + \frac{p_{1z}+p_{2z}}{\sqrt{p_{1r}p_{2r}}}\mathcal{A}_1\mathcal{A}_2\mathrm{Re}(Y_{lm}(\beta_1,\phi)Y_{lm}^*(\beta_2,\phi)) \\ & \times \cos\left(\Delta S - \frac{\pi}{2}\right)\Bigg\}. \end{aligned} \tag{D6}$$

For $z \gg d$, the results for the plane detector can be obtained from the results for the spherical detector by using $p_{\nu z} = p_{\nu r}\cos\theta, j_z = j_r\cos\theta$, and $\widetilde{j}_z = \widetilde{j}_r\cos^3\theta$.

APPENDIX E: EXACT COULOMB GREEN'S FUNCTION METHOD FOR AN *S*-WAVE SOURCE

The exact Coulomb Green's function can be written as [11]

$$\begin{aligned} G(\mathbf{r},\mathbf{d},\epsilon) = \frac{\Gamma(1-i\iota)}{2\pi|\mathbf{r}-\mathbf{d}|} & [\mathcal{W}'_{i\iota,1/2}(\varrho)\mathcal{M}_{i\iota,1/2}(\vartheta) \\ & - \mathcal{W}_{i\iota,1/2}(\varrho)\mathcal{M}'_{i\iota,1/2}(\vartheta)], \end{aligned} \tag{E1}$$

which satisfies the inhomogeneous Schrödinger equation with a delta source,

$$\left(\frac{1}{2}\nabla^2 - \frac{\alpha}{r} + \epsilon\right)G(\mathbf{r},\mathbf{d},\epsilon) = \delta(\mathbf{r}-\mathbf{d}), \tag{E2}$$

where, $\epsilon = E + \alpha/d$ and $\iota = -\alpha/\kappa$ with $\kappa = \sqrt{2\epsilon}$; $\varrho = -i\kappa(r + d + |\mathbf{r}-\mathbf{d}|)$, and $\vartheta = -i\kappa(r + d - |\mathbf{r}-\mathbf{d}|)$; $\Gamma(1-i\iota)$ is a gamma function [16]; $\mathcal{M}_{i\iota,1/2}(\vartheta)$ and $\mathcal{W}_{i\iota,1/2}(\varrho)$ are, respectively, the Whittaker functions of the first kind and the second kind [16].

Based on the above Coulomb Green's function, an exact quantum-mechanical flux generated by an s-wave source can be obtained from Eq. (41),

$$j_r = \frac{|\Gamma(1-i\iota)|^2}{4\pi^2|\mathbf{r}-\mathbf{d}|^2}\mathrm{Im}(\Phi^*\Psi), \tag{E3}$$

where

$$\Phi = \mathcal{W}'_{i\iota,1/2}(\varrho)\mathcal{M}_{i\iota,1/2}(\vartheta) - \mathcal{W}_{i\iota,1/2}(\varrho)\mathcal{M}'_{i\iota,1/2}(\vartheta), \tag{E4}$$

and

$$\begin{aligned} \Psi = & \mathcal{W}''_{i\iota,1/2}(\varrho)\mathcal{M}_{i\iota,1/2}(\vartheta)\frac{\partial\varrho}{\partial r} \\ & + \mathcal{W}'_{i\iota,1/2}(\varrho)\mathcal{M}'_{i\iota,1/2}(\vartheta)\left(\frac{\partial\vartheta}{\partial r} - \frac{\partial\varrho}{\partial r}\right) \\ & - \mathcal{W}_{i\iota,1/2}(\varrho)\mathcal{M}''_{i\iota,1/2}(\vartheta)\frac{\partial\vartheta}{\partial r}, \end{aligned} \tag{E5}$$

with [16]

$$\mathcal{W}''_{i\iota,1/2}(\varrho) = \left(\frac{1}{4} - \frac{i\iota}{\varrho}\right)\mathcal{W}_{i\iota,1/2}(\varrho); \tag{E6}$$

$$\mathcal{M}''_{i\iota,1/2}(\vartheta) = \left(\frac{1}{4} - \frac{i\iota}{\vartheta}\right)\mathcal{M}_{i\iota,1/2}(\vartheta); \tag{E7}$$

$$\mathcal{W}'_{i\iota,1/2}(\varrho) = -\frac{1}{\varrho}\mathcal{W}_{i\iota+1,1/2}(\varrho) + \left(\frac{1}{2} - \frac{i\iota}{\varrho}\right)\mathcal{W}_{i\iota,1/2}(\varrho); \tag{E8}$$

$$\mathcal{M}'_{i\iota,1/2}(\vartheta) = \frac{i\iota+1}{\vartheta}\mathcal{M}_{i\iota+1,1/2}(\vartheta) + \left(\frac{1}{2} - \frac{i\iota}{\vartheta}\right)\mathcal{M}_{i\iota,1/2}(\vartheta). \tag{E9}$$

The free-electron Green's function satisfies

$$\left(\tfrac{1}{2}\nabla^2+E\right)G_{\rm free}(\mathbf{r},\mathbf{d},E)=\delta(\mathbf{r}-\mathbf{d}), \tag{E10}$$

and has the following expression,

$$G_{\rm free}(\mathbf{r},\mathbf{d},E)=-\frac{e^{ik|\mathbf{r}-\mathbf{d}|}}{2\pi|\mathbf{r}-\mathbf{d}|}, \tag{E11}$$

which serves as a reference for the initial outgoing wave. Following the definition in Eq. (46) in Sec. IV, the reduced expression for the exact quantum flux on a spherical detector of radius r can be written as

$$\tilde{j}_r=\frac{r^2}{\sqrt{2E}|\mathbf{r}-\mathbf{d}|^2}|\Gamma(1-i\iota)|^2\mathrm{Im}(\Phi^*\Psi). \tag{E12}$$

In Figs. 6(a)–6(f), the above formula in Eq. (E12) has been compared with the semiclassical result in Eq. (52) for the s wave. The agreement between the two independent approaches indicates that both results are reliable.

We have also found as the detection distance increases, the computation using Eq. (E12) becomes more and more difficult because of the Whittaker function of the second kind. However, it is possible to simplify the expressions in the large r limit. Note when $r \gg d$, Eqs. (E6) and (E8) can be simplified to

$$\mathcal{W}''_{i\iota,1/2}(\varrho)\doteq\frac{1}{4}\mathcal{W}_{i\iota,1/2}(\varrho); \tag{E13}$$

$$\mathcal{W}'_{i\iota,1/2}(\varrho)\doteq-\frac{1}{\varrho}\mathcal{W}_{i\iota+1,1/2}(\varrho)+\frac{1}{2}\mathcal{W}_{i\iota,1/2}(\varrho). \tag{E14}$$

In addition, when $r \gg d$, we have $|\varrho| \gg 1$. The following two approximations related to the Whittaker function of the second kind [17] can be used,

$$\mathcal{W}_{i\iota,1/2}(\varrho)\doteq\varrho^{i\iota}e^{-\varrho/2}, \tag{E15}$$

and

$$\mathcal{W}_{i\iota+1,1/2}(\varrho)\doteq\varrho\mathcal{W}_{i\iota,1/2}(\varrho). \tag{E16}$$

The detached-electron flux on a spherical detector can be written as

$$j_r=\frac{\kappa e^{\iota\pi}|\Gamma(1-i\iota)|^2}{4\pi^2|\mathbf{r}-\mathbf{d}|^2}\times\left|\mathcal{M}'_{i\iota,1/2}(\vartheta)+\frac{1}{2}\mathcal{M}_{i\iota,1/2}(\vartheta)\right|^2. \tag{E17}$$

Note that the exponential contains ι, not i.

When Eq. (E9) is used, the above expression can be written alternatively as

$$j_r=\frac{e^{\iota\pi}|\Gamma(1-i\iota)|^2}{4\kappa\pi^2|\mathbf{r}-\mathbf{d}|^2}\times\frac{|i\iota\mathcal{M}_{i\iota,1/2}(\vartheta)-(i\iota-1)\mathcal{M}_{i\iota-1,1/2}(\vartheta)|^2}{d^2(1+\cos\theta)^2}, \tag{E18}$$

where the following recurrence relation was also needed [18],

$$(i\iota-1)\mathcal{M}_{i\iota-1,1/2}(\vartheta)+(\vartheta-2i\iota)\mathcal{M}_{i\iota,1/2}(\vartheta)+(i\iota+1)\mathcal{M}_{i\iota+1,1/2}(\vartheta)=0. \tag{E19}$$

Using a relationship between the Whittaker function and the Kummer function [16],

$$\mathcal{M}_{\tilde{\mu},\tilde{\eta}}(\vartheta)=e^{-\vartheta/2}\vartheta^{\frac{1}{2}+\tilde{\eta}}M\left(\tfrac{1}{2}+\tilde{\eta}-\tilde{\mu},1+2\tilde{\eta},\vartheta\right), \tag{E20}$$

the expression in Eq. (E18) can be written alternatively as

$$j_r=\frac{\kappa e^{\iota\pi}|\Gamma(1-i\iota)|^2}{4\pi^2|\mathbf{r}-\mathbf{d}|^2}\times|i\iota M(1-i\iota,2,\vartheta)-(i\iota-1)M(2-i\iota,2,\vartheta)|^2. \tag{E21}$$

Furthermore using a recurrence relation for the Kummer functions [18],

$$M(1-i\iota,1,\vartheta)-i\iota M(1-i\iota,2,\vartheta)-(1-i\iota)M(2-i\iota,2,\vartheta)=0, \tag{E22}$$

the above expression in Eq. (E21) can be simplified as

$$j_r=\frac{\kappa\iota e^{\iota\pi}}{4\pi\sinh(\iota\pi)|\mathbf{r}-\mathbf{d}|^2}\times|M(1-i\iota,1,\vartheta)|^2, \tag{E23}$$

where the explicit expression for $|\Gamma(1-i\iota)|^2$ has been used [16].

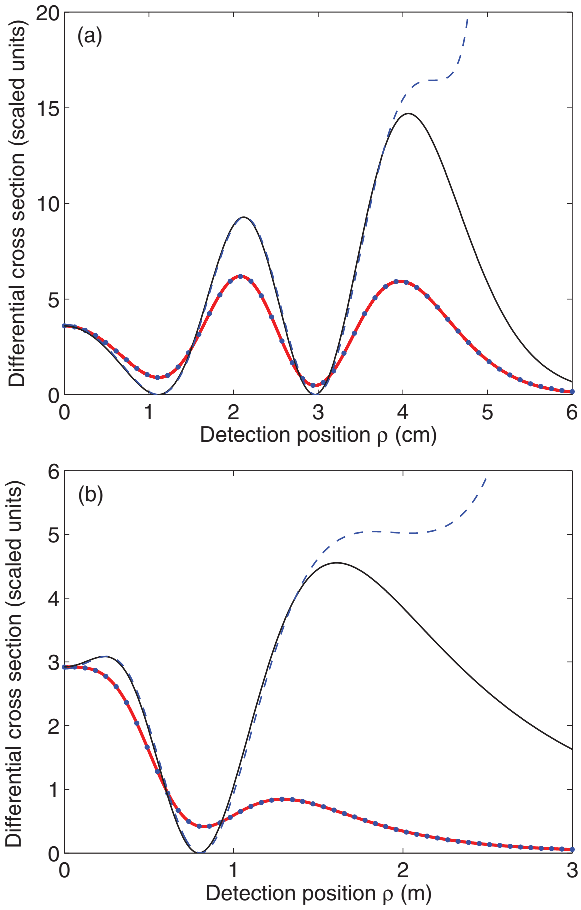

FIG. 11. (Color online) Comparing calculations from different approaches. The red and thick lines are from the present semiclassical propagation method [Eq. (D6) and its extension into the classically forbidden region], and the dots represent the calculations from the Coulomb Green's function we derived in Appendix E [Eq. (E27)]. We emphasize the above two approaches are independent of each other. The results given in Eq. (E28) [19] are displayed by the thin solid curves. Note the calculations are matched with our results at the point $\rho = 0$. The one-dimensional WKB approximation of $M_{i\iota,1/2}(\vartheta)$ [19] described in Appendix E are the dashed lines. (a) $z = 5$ cm, $E = 0.1$ cm^{-1}, $d = 66100a_0$, and $\tilde{E} = 0.16925$. (b) $d = 300a_0$, $\alpha = 1$, $z = 1m$, and $\tilde{E} = 0.5$.

Finally, when $r \gg d$, from Eq. (E23) and using the relationship between the Whittaker function and the Kummer function in Eq. (E20) again, the expression in Eq. (E3) is simplified to

$$j_r = \frac{\iota e^{\iota\pi}}{4\pi\,\sinh(\iota\pi)|\mathbf{r}-\mathbf{d}|^2} \times \frac{|\mathcal{M}_{i\iota-1/2,0}(\vartheta)|^2}{d(1+\cos\theta)}, \tag{E24}$$

and the reduced flux in Eq. (E12) can be written as

$$\tilde{j}_r = \frac{\iota\pi e^{\iota\pi}}{\sqrt{2E}\,\sinh(\iota\pi)} \times \frac{|\mathcal{M}_{i\iota-1/2,0}(\vartheta)|^2}{d(1+\cos\theta)}. \tag{E25}$$

For a plane detector at $z \gg d$, the reduced flux is described by

$$j_z = \frac{\iota e^{\iota\pi}}{4\pi\,\sinh(\iota\pi)|\mathbf{r}-\mathbf{d}|^2} \times \frac{\cos\theta}{d(1+\cos\theta)} \times |\mathcal{M}_{i\iota-1/2,0}(\vartheta)|^2, \tag{E26}$$

and the corresponding reduced flux in Eq. (D5) can be obtained as

$$\tilde{j}_z = \frac{\iota\pi e^{\iota\pi}}{\sqrt{2E}\,\sinh(\iota\pi)} \times \frac{(\cos\theta)^3}{d(1+\cos\theta)} \times |\mathcal{M}_{i\iota-1/2,0}(\vartheta)|^2. \tag{E27}$$

Note the first subscript in the Whittaker function is $i\iota - 1/2$, not $i\iota$.

When this work was nearly complete, we noticed that Golovinski and Drobyshev have also examined the present model for an s-wave source based on the Coulomb Green's function [19]. However, they obtained

$$j_z \sim |\mathcal{M}_{i\iota,1/2}(\vartheta)|^2, \tag{E28}$$

which differs from our result in Eq. (E26). Golovinski and Drobyshev also used a semiclassical approximation to calculate Whittaker's equation $\mathcal{M}_{i\iota,1/2}(\vartheta)$. Note that the Whittaker function $\mathcal{M}_{i\iota,1/2}(\vartheta)$ satisfies the following Whittaker's equation [16],

$$\frac{d^2\mathcal{M}_{i\iota,1/2}(\vartheta)}{d\vartheta^2} - \left(\frac{1}{4} - \frac{i\iota}{\vartheta}\right)\mathcal{M}_{i\iota,1/2}(\vartheta) = 0, \tag{E29}$$

which can be written as

$$\frac{d^2\mathcal{M}_{i\iota,1/2}(\vartheta)}{dy^2} + \left(\kappa^2 - \frac{2\alpha}{y}\right)\mathcal{M}_{i\iota,1/2}(\vartheta) = 0, \tag{E30}$$

where

$$y = \tfrac{1}{2}(r + d - |\mathbf{r}-\mathbf{d}|). \tag{E31}$$

Equation (E30) corresponds to a one-dimensional Schrödinger equation for a particle with energy $\epsilon = \frac{\kappa^2}{2}$ in a potential $V(y) = \frac{\alpha}{y}$. Therefore, the semiclassical approximation or the WKB approximation can be obtained [19] as

$$\mathcal{M}^{\mathrm{WKB}}_{i\iota,1/2}(\vartheta) \sim \frac{1}{\kappa^{1/2}(1-\frac{1}{s})^{1/4}}\sin\left[S(y) + \frac{\pi}{4}\right], \quad y > y_0, \tag{E32}$$

where,

$$S(y) = \kappa y_0[\sqrt{s(s-1)} - \ln(\sqrt{s-1} + \sqrt{s})], \tag{E33}$$

and $s = y/y_0$ with $y_0 = \alpha/\epsilon$ being the turning point.

In Fig. 11 our results are compared with the results of Golovinski and Drobyshev [19]. While the WKB approximations (dashed lines) are rather good to reproduce the differential cross sections in Eq. (E28) (blue and thin lines) [19] in the small ρ region, their results, however, differ significantly from ours. Our calculations using the three-dimensional semiclassical propagation approach (red and thick lines) agree well with the results based on Coulomb Green's function (dots). And, furthermore, these two approaches are independent.

---

[1] X. P. Xing, X. B. Wang, and L. S. Wang, Phys. Rev. Lett. **101**, 083003 (2008); J. Chem. Phys. **130**, 074301 (2009).

[2] I. I. Fabrikant, Sov. Phys.-JETP **52**, 1045 (1980).

[3] Y. N. Demkov, V. D. Kondratovich, and V. N. Ostrovskii, JETP Lett. **34**, 403 (1981).

[4] M. L. Du, Phys. Rev. A **40**, 4983 (1989).

[5] C. Blondel, C. Delsart, and F. Dulieu, Phys. Rev. Lett. **77**, 3755 (1996).

[6] M. L. Du and J. B. Delos, Phys. Rev. A **38**, 5609 (1988); Phys. Lett. A **134**, 476 (1989); M. L. Du, Phys. Rev. A **70**, 055402 (2004); Eur. Phys. J. D **38**, 533 (2006).

[7] M. L. Du, Phys. Rev. A **40**, 1330 (1989); A. D. Peters and J. B. Delos, *ibid.* **47**, 3020 (1993); **47**, 3036 (1993); A. D. Peters, C. Jaffé, and J. B. Delos, Phys. Rev. Lett. **73**, 2825 (1994); Phys. Rev. A **56**, 331 (1997); A. D. Peters, C. Jaffé, J. Gao, and J. B. Delos, *ibid.* **56**, 345 (1997); C. Bracher and J. B. Delos, Phys. Rev. Lett. **96**, 100404 (2006); C. Bracher, T. Kramer, and J. B. Delos, Phys. Rev. A **73**, 062114 (2006).

[8] H. C. Bryant *et al.*, Phys. Rev. Lett. **58**, 2412 (1987); J. E. Stewart *et al.*, Phys. Rev. A **38**, 5628 (1988); P. G. Harris *et al.*, *ibid.* **41**, 5968 (1990); N. D. Gibson, B. J. Davies, and D. J. Larson, *ibid.* **47**, 1946 (1993); **48**, 310 (1993); N. D. Gibson, M. D. Gasda, K. A. Moore, D. A. Zawistowski, and C. W. Walter, *ibid.* **64**, 061403(R) (2001); J. N. Yukich, T. Kramer, and C. Bracher, *ibid.* **68**, 033412 (2003); W. Chaibi, R. J. Peláez, C. Blondel, C. Drag, and C. Delsart, Eur. Phys. J. D **58**, 29 (2010) and references therein.

[9] A. R. P. Rau and Hin-Yiu Wong, Phys. Rev. A **37**, 632 (1988); Hin-Yiu Wong, A. R. P. Rau, and C. H. Greene, *ibid.* **37**, 2393 (1988); I. I. Fabrikant, *ibid.* **43**, 258 (1991).

[10] M. L. Du and J. B. Delos, Phys. Rev. Lett. **58**, 1731 (1987); Phys. Rev. A **38**, 1896 (1988); **38**, 1913 (1988).

[11] L. Hostler and R. H. Pratt, Phys. Rev. Lett. **10**, 469 (1963); L. Hostler, J. Math. Phys. **5**, 591 (1964); **5**, 1235 (1964).

[12] S. M. Blinder, J. Math. Phys. **22**, 306 (1981); Int. J. Quantum Chem. **26**(S18), 293 (1984).

[13] H. Goldstein, *Classical Mechanics* (Addison-Wesley, London, 1980).

[14] V. P. Maslov and M. V. Fedoriuk, *Semi-Classical Approximation in Quantum Mechanics* (Reidel, Boston, 1981); M. C.

Gutzwiller, J. Math. Phys. **12**, 343 (1971); J. B. Delos, Adv. Chem. Phys. **65**, 161 (1986).

[15] M. S. Child, *Semiclassical Mechanics with Molecular Application* (Clarendon, Oxford, 1991).

[16] M. Abramawitz and I. A. Stegun, eds., *Handbook of Mathematical Functions with Formulas, Graphs, and Mathematical Tables* (Dover, New York, 1965).

[17] I. S. Gradshteyn and I. M. Ryzhik, *Table of Integrals, Series, and Products* (Academic Press, New York, 1980).

[18] F. W. J. Olver, D. W. Lozier, R. F. Boisvert, and C. W. Clark, *NIST Handbook of Mathematical Functions* (Cambridge University Press, New York, 2010).

[19] P. A. Golovinski and A. A. Drobyshev, Proc. SPIE **7993**, 799311 (2011).